Strong acoustic plasmons in chemically doped graphene induced by a nearby metal surface

Vito Despoja,[1,4,*] Dino Novko,[1,4] Ivor Lončarić,[2,4] Neven Golenić,[1] Leonardo Marušić,[3] and Vyacheslav M. Silkin[4,5,6]

[1]*Institute of Physics, Bijenička 46, HR-10000 Zagreb, Croatia*

[2]*Ruđer Bošković Institute, Bijenička 54, HR-10000 Zagreb, Croatia*

[3]*Maritime Department, University of Zadar, M. Pavlinovića 1, HR-23000 Zadar, Croatia*

[4]*Donostia International Physics Center, P. Manuel de Lardizabal, 4, 20018 San Sebastián, Spain*

[5]*Departamento de Fisica de Materiales and Centro Mixto CSIC-UPV/EHU, Facultad de Ciencias Químicas, Universidad del Pais Vasco UPV/EHU, Apto. 1072, 20080 San Sebastián, Spain*

[6]*IKERBASQUE, Basque Foundation for Science, 48013 Bilbao, Spain*

(Received 17 July 2019; revised manuscript received 19 October 2019; published 4 November 2019)

Recent theoretical considerations have demonstrated that free-standing graphene doped with alkali metals (AC_x) supports strong Dirac and weak acoustic plasmons. Here we show that when AC_x is deposited on a metal surface the effective Coulomb screening produced by the substrate can completely wash out these collective modes. However, even tiny detachment of the AC_x layer from the metal surface recovers the AC_x plasmonic properties. Especially the acoustic plasmon intensity is strongly enhanced in comparison to a free-standing case. We further provide the physical background of these intriguing phenomena. The studied systems consist of lithium- and cesium-doped graphene layers deposited on the Ir(111) surface.

DOI: 10.1103/PhysRevB.100.195401

I. INTRODUCTION

Ground-state crystal and electronic structures of graphene doped with alkali-metal atoms (AC_x, A = Li, Na, K, Cs) on different metallic surfaces, such as Ir(111), Cu(111), and Ni(111), have been recently extensively studied in several experimental and/or theoretical papers [1–7]. The goal of these investigations was to achieve free-standing graphene (decoupled from the surface as much as possible) with the smallest moiré corrugation. Moreover, the above-mentioned experiments and further density functional theory (DFT) calculations [8] showed that graphene doped by alkali-metal atoms possesses an electronic band structure that could potentially support very interesting plasmonic properties. This is related to the fact that the alkali-metal atoms in a two-dimensional (2D) superlattice become metallic and form a parabolic electronic σ band that crosses the Fermi level [9]. Moreover, the alkali-metal atoms donate electrons to the graphene π band, lifting the Fermi level to more than 1 eV above the Dirac point [8]. As a result, coexistence of these partially occupied 2D energy bands in AC_x could support at least two electronic collective modes, where one is supposed to be a very strong Dirac plasmon (DP) [10,11].

The main goal of this paper is to emphasize the plasmonic effects existing in free-standing graphene doped by alkali metals. Recent theoretical investigations [12,13] have already reported on a strong DP and a weak acoustic plasmon (AP) [14,15] in AC_x. However, here we focus on a much more realistic situation where doped graphene is deposited on metal surfaces [16–21]. Especially we aim to explore how the vicinity of the metal surface can be used to modify the DP and AP dispersion relations and intensities. Investigation of graphene-metal heterostructures is actually of both fundamental [22] and practical [23,24] importance. For instance, in the field of graphene-based biosensing [24] the graphene-metal contacts are unavoidable and thus deciphering the microscopic screening mechanisms in these structures is of great value.

In this paper we investigate the low-energy collective electronic excitations (2D plasmons) in lithium- and cesium-doped graphene (i.e., LiC_2 and CsC_8) deposited on the Ir(111) surface. Special attention is paid to explore how the vicinity of the Ir(111) surface modifies the DP properties and enhances the AP intensities. We show how free-standing doped graphene supports a very strong DP and an AP with intensity weaker by two orders of magnitude. When the AC_x layer is located at the equilibrium position at the Ir(111) surface, the strong metallic screening in the substrate destroys the corresponding plasmonic excitations such that the DP in LiC_2 becomes a very weak acousticlike branch, while the DP in CsC_8 almost completely disappears. However, a small upward vertical displacement of the AC_x layer from the equilibrium position recovers the low-energy plasmon modes. Moreover this gives birth to interesting plasmonic phenomena not present in free-standing doped graphene. For instance, at a vertical displacement Δ of 0.6–1.2 Å a very strong AP branch appears in LiC_2. At displacement Δ of 1.2–1.6 Å the CsC_8/Ir(111) supports two intense AP modes. At finite momentum transfers ($Q > 0.1$ a.u.) the intensities of these APs (lying in the infrared frequency range, $\omega > 1$ eV) can be even two orders of magnitude stronger than the DP intensities in the free-standing AC_x layer. These very intriguing plasmonic phenomena can be of interest in many plasmonics applications [25–36].

The rest of the paper is organized as follows. In Sec. II A we present a theoretical model for the ground-state crystal

*vito@phy.hr

and electronic structure of the LiC_2/Ir(111) and CsC_8/Ir(111) systems. In Sec. II B we describe the method for calculating the effective 2D dielectric function $\epsilon(\mathbf{Q}, \omega)$ of AC_x/Ir(111). In Sec. III the results for the calculated energy-loss function (ELF) $-\mathrm{Im}[\epsilon^{-1}]$ and real part of the effective 2D dielectric function $\mathrm{Re}[\epsilon]$ in AC_x/Ir(111) are presented. Finally, we provide the conclusions in Sec. IV. When not stated otherwise, atomic units are used, i.e., $e = \hbar = m_e = 1$, where e is the electronic charge, $\hbar$ is the reduced Plank constant, and m_e is the mass of the electron.

II. THEORETICAL MODEL

A. Ground-state calculation

The studied systems consist of a graphene monolayer doped with alkali-metal atoms and deposited on the Ir(111) surface [AC_x/Ir(111) composite], as shown in Fig. 1. The separation between the alkali-metal atom layer in AC_x and the topmost Ir atomic layer of Ir(111) is

$$h = d_{\text{Ir-}A} + \Delta,$$

where $d_{\text{Ir-}A}$ represents the equilibrium separation obtained from the DFT calculations and Δ represents the vertical displacement from the equilibrium position.

The crystal structure of the Ir(111) surface is modeled with five atomic layers. A graphene 2×2 superlattice is matched to a Ir(111) $\sqrt{3} \times \sqrt{3}$ superlattice such that 4.8% strain is applied to Ir(111). The unit cell in the z direction is set to $L = 22$ Å.

Ground-state electronic and structural optimization calculations were performed using the QUANTUM ESPRESSO package [37,38]. The core-electron interaction is approximated by the norm-conserving pseudopotentials [39]. In order to capture the long-range van der Waals (vdW) interaction between the Ir(111) surface and doped graphene layers we use the vdW exchange-correlation functional [40,41], in particular the vdW-DF-cx version [42,43]. The ground-state properties in AC_x/Ir(111) composites are calculated by using the $9 \times 9 \times 1$ Monkhorst-Pack K-point mesh [44], and the plane-wave cutoff energy is chosen to be 60 Ry. The structural optimization calculations are performed until the maximum force on each atom is reduced below 0.002 eV/Å.

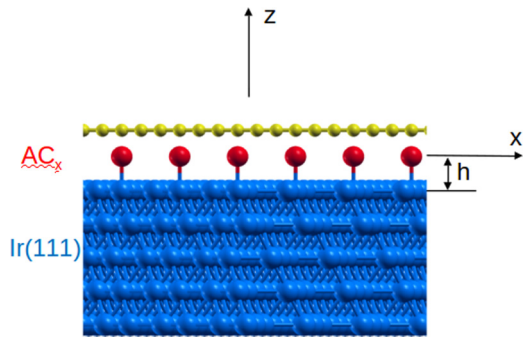

FIG. 1. Crystal structure of the alkali-metal atom doped graphene monolayer deposited on the Ir(111) surface [an AC_x/Ir(111) composite].

TABLE I. The equilibrium separations (in Å) between the topmost iridium atomic layer and the alkali-metal atom layer $d_{\text{Ir-}A}$ as well as between the alkali-metal atom layer and the graphene monolayer $d_{A\text{-C}}$ in the AC_x/Ir(111) composites. The Fermi energies (in eV) are relative to the graphene Dirac point.

	LiC_2	CsC_8	LiC_2/Ir(111)	CsC_8/Ir(111)
$d_{\text{Ir-}A}$			2.4	2.97
$d_{A\text{-C}}$	2.17	3.0	1.9	3.17
E_F	1.78	1.24	1.61	0.95

The investigation of the plasmonic properties of the AC_x/Ir(111) system is performed by treating the doped graphene AC_x and the Ir(111) surfaces as nonoverlapping or chemically independent systems interacting by the long-range Coulomb potential. The Fermi levels in LiC_2 and CsC_8 samples, relative to the graphene Dirac point, are then frozen to their self-standing ($h \to \infty$) values E_F=1.78 and 1.24 eV, respectively, regardless of the separation h. The *ab initio* calculations of the entire AC_x/Ir(111) system in equilibrium ($h = d_{\text{Ir-}A}$) give slightly lower values, E_F=1.61 and 0.95 eV. However, the influence of such a small change in the Fermi level on the AC_x plasmonic properties is negligible. The obtained vertical equilibrium separations between different atomic layers and Fermi levels (relative to the graphene Dirac point) in the AC_x/Ir(111) composites are listed in Table I.

B. Calculation of an effective 2D dielectric function

Large equilibrium distance $d_{\text{Ir-}A}$ results in small electronic overlap between the AC_x slab and the Ir(111) topmost layer which allows us to separate the calculation of the dynamically screened Coulomb interaction into two independent calculations, namely, computation of the AC_x noninteracting electron response function $\chi^0_{AC_x}$ and Ir(111) surface response function D_{Ir}. Such approach considerably reduces the unit-cell size and tremendously saves the computational time and memory requirements. This is indeed quite useful for studying the dynamical response in the AC_x/Ir(111) composite when the AC_x-Ir(111) distance is much larger than the equilibrium separation $h \gg d_{\text{Ir-}A}$.

The ground-state electronic structures of LiC_2 and CsC_8 are first calculated using the equilibrium positions $d_{A\text{-C}}$ as in the AC_x/Ir(111) composite (see Table I) and using other parameters as described in Ref. [45]. The noninteracting electron response functions $\chi^0_{AC_x}$ are calculated using dense K-point grids, i.e., $201 \times 201 \times 1$ and $101 \times 101 \times 1$ K-point meshes for LiC_2 and CsC_8, respectively. The band summations in $\chi^0_{AC_x}$ are performed over 30 and 100 bands, for LiC_2 and CsC_8, respectively. In both cases the damping parameter $\eta = 20$ meV is used. The calculation of the $\chi^0_{AC_x}$ is performed by fixing the Fermi energies E_F and the separations $d_{A\text{-C}}$ to the self-standing ($h \to \infty$) values, as stated in the two left columns of Table I. It should be noted here that for response function calculations the crystal local-field effects are included only in the perpendicular (z) direction, i.e., the response functions are nonlocal only in the perpendicular direction and can be Fourier transformed as $\chi(z, z') = \frac{1}{L} \sum_{G_z G'_z} e^{iG_z z - iG'_z z'} \chi_{G_z G'_z}$ where G_z and G'_z the are reciprocal-lattice vectors in the

perpendicular direction. For $\chi^0_{AC_x}$ calculations we use a crystal local-field energy cutoff of 10 Ry, which corresponds to 23 G_z wave vectors. The dynamically screened Coulomb interaction can be calculated by solving the Dyson equation $w = v + v \otimes \chi^0_{AC_x} \otimes w$, where $v = (2\pi/Q)e^{-Q|z-z'|}$ is bare Coulomb interaction [48] and $\otimes \equiv \int_\infty^\infty dz$.

In the vicinity of the polarizable Ir(111) surface the Coulomb interaction (e.g., the interaction between charge density fluctuations at $z, z' > -h$) is mediated by the surface screened Coulomb interaction instead of the bare interaction v:

$$w_{\rm Ir} = v + \frac{2\pi}{Q} D_{\rm Ir}\, e^{-2Qh} e^{-Q(z+z')},$$

where $D_{\rm Ir} = \frac{2\pi}{Q}\langle e^{Qz_1}|\chi_{\rm Ir}(\mathbf{Q},\omega,z_1,z_2)|e^{Qz_2}\rangle$ is the Ir(111) surface response function. The Ir(111) response function $\chi_{\rm Ir}$ can be obtained by solving Dyson equation $\chi_{\rm Ir} = \chi^0_{\rm Ir} + \chi^0_{\rm Ir} \otimes v \otimes \chi_{\rm Ir}$, where $\chi^0_{\rm Ir}$ represents the Ir(111) noninteracting electron response function. The ground-state electronic structure of the Ir(111) surface [45] is calculated using the 1×1 unit cell. The response function $\chi^0_{\rm Ir}$ is calculated using $101 \times 101 \times 1$ K-point mesh, and the band summation is performed over 150 bands. The damping parameter $\eta = 30$ meV is used. The crystal local-field energy cutoff of 10 Ry is used, which equal to the 37 G_z wave vectors.

After the AC_x is deposited on the polarizable Ir(111) surface the bare Coulomb interaction v has to be replaced by the surface screened Coulomb interaction ($v \rightarrow w_{\rm Ir}$), and the dynamically screened Coulomb interaction of the entire AC_x/Ir(111) composite is calculated by solving the "screened" Dyson equation:

$$w = w_{\rm Ir} + w_{\rm Ir} \otimes \chi^0_{AC_x} \otimes w. \tag{1}$$

Finally, the effective 2D dielectric function can be defined as

$$\epsilon^{-1}(\mathbf{Q},\omega) = w(\mathbf{Q},\omega,z=0,z'=0)/v_Q,$$

where $v_Q = 2\pi/Q$. The energy-loss function directly probed in the reflection electron-energy-loss experiment [49] is then calculated as the imaginary part of ϵ^{-1}, $S(\mathbf{Q},\omega) = -(1/\pi)\mathrm{Im}[\epsilon^{-1}(\mathbf{Q},\omega)]$.

C. Long-wavelength limit $Q \approx 0$

Due to the strong dispersivity of the dielectric response in the perpendicular (z) direction it is not possible to neglect the crystal local-field effects in that direction and use the local 2D representation of the AC_x dielectric response. For example, the AP can be interpreted as an out-of-phase charge density oscillation in the alkali-metal atom (A) and the graphene (C) plane, as has been theoretically demonstrated [12]. A similar plasmon has also been experimentally observed, propagating in the graphene/hBN/metallic rod heterostructure [23]. Therefore, neglecting the crystal local-field effects for such layered heterostructures (which is equivalent to averaging in the z direction) would remove the AP from the electron-energy-loss spectroscopy (EELS) spectrum. However, in the long-wavelength limit ($Q \rightarrow 0$), the local 2D representation can be used even if the crystal local-field effects are neglected, by considering the AC_x layer as two 2D sheets, A and C, separated by $d_{A\text{-}C}$ and described by their local 2D dielectric functions $\epsilon_A(\omega)$ and $\epsilon_C(\omega)$, respectively. Similar attempts have been successful in the experimental investigation [23]. In that case the effective 2D dielectric function of A-C sheets can be written as

$$\epsilon^0_{\rm 2D} = \epsilon_A \frac{1 - \alpha_C \alpha_A e^{-2Qd_{A\text{-}C}}}{1 + \alpha_C e^{-2Qd_{A\text{-}C}}}. \tag{2}$$

Here $\alpha_i = \frac{1-\epsilon_i}{\epsilon_i}$, the 2D dielectric function of a particular sheet is $\epsilon_i = 1 - \frac{2\pi}{Q}\chi^0_i(Q,\omega)$, and the 2D response function is $\chi^0_i(Q,\omega) = L_i\ \chi^0_{i,G_z=0G'_z=0}(Q,\omega)$, where $i = $ C or A. $\chi^0_{i,G_zG'_z}(Q,\omega)$ are the *ab initio* noninteracting electron response functions of separated atomic ($i = A$) and graphene ($i = $ C) layers, where L_i represents the unit-cell constant in the perpendicular direction. The χ^0_i can also be obtained in a simpler model, such as the Dirac-cone approach [11] for $i = $ C and one parabolic 2D band for $i = A$ [12]. This A-C sheet 2D model dielectric function does not include the dispersivity of the dynamical response perpendicular to the C and A layers and it does not include intersystem (C $\leftrightarrow$ A) electron-hole excitations. However, both effects are very small in the $Q \approx 0$ limit, and so Eq. (2) probably provides good AP and DP dispersion relations. In the presence of the iridium surface the effective dielectric function of the A-C sheets becomes

$$\epsilon^{\rm Ir}_{\rm 2D} = \frac{1 - \alpha_{\rm 2D} D_{\rm Ir} e^{-2Qh}}{1 + \alpha_{\rm 2D} + D_{\rm Ir} e^{-2Qh} + \alpha_{\rm 2D} D_{\rm Ir} e^{-2Qh}}, \tag{3}$$

where $\alpha_{\rm 2D} = \frac{1-\epsilon^0_{\rm 2D}}{\epsilon^0_{\rm 2D}}$. For larger separations $h \gg d_{\text{Ir-}A}$, which corresponds to the long-wavelength limit ($Q \approx \frac{1}{h}$), the Ir(111) surface response function can be approximated as

$$D_{\rm Ir} = \frac{1 - \epsilon_{\rm Ir}}{1 + \epsilon_{\rm Ir}} \tag{4}$$

where $\epsilon_{\rm Ir}$ represents, for example, the bulk iridium macroscopic dielectric function. For smaller separations $h \approx d_{\text{Ir-}A}$, the quantum nonlocal effects are important and the local description (4) becomes inaccurate. Therefore, the model 2D dielectric functions (2)–(4) possibly provide good DP and AP dispersion relations in the long-wavelength $Q \approx 0$ and $h \gg d_{\text{Ir-}A}$ limits, however it cannot be expected that they could give good AP and DP oscillatory strengths (e.g., their relative intensities), which is the main objective of this investigation.

III. RESULTS AND DISCUSSION

First we describe the modifications produced in the electronic excitation spectra of the AC_x layer when it is brought from a free-standing ($\Delta \rightarrow \infty$) to the equilibrium ($\Delta = 0$) distance at the Ir(111) slab. In addition, gradually increasing the separation $\Delta > 0$, we present the corresponding spectra and explain the physical background of spectral alterations.

Figure 2(a) shows the ELF intensity in free-standing ($\Delta = \infty$) LiC_2. As already reported in Ref. [12], in LiC_2 the Li atoms donate electrons to the graphene π^* band and additionally they form a parabolic σ band which remains partially filled. Therefore, there are two bands crossing the Fermi level which result in two plasmons in LiC_2, i.e., a strong DP and a weak AP [see Fig. 2(a)] as is the case in

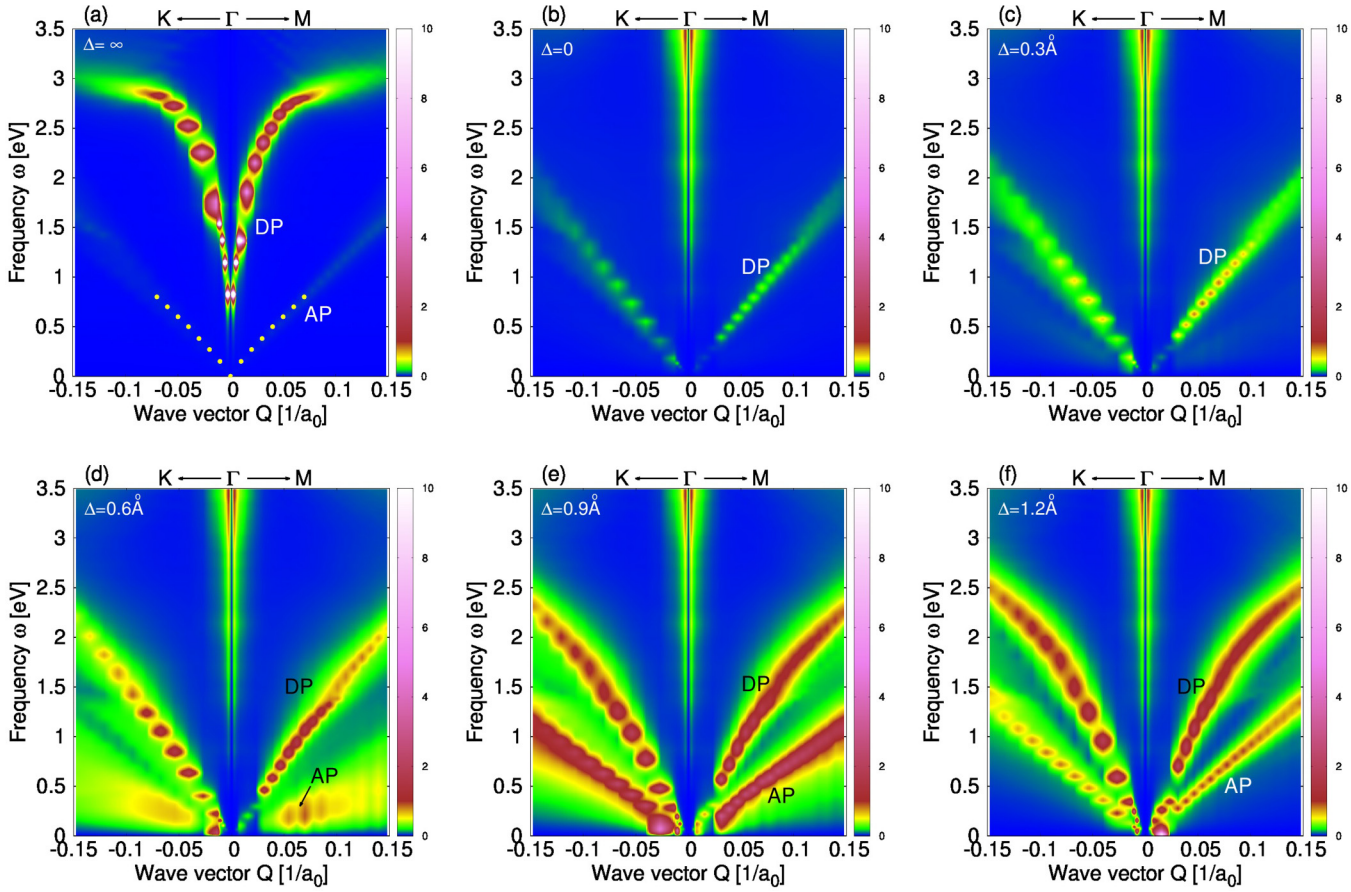

FIG. 2. The energy-loss-function intensity in LiC_2/Ir(111) composite for (a) $\Delta = \infty$, (b) $\Delta = 0$, (c) $\Delta = 0.3$ Å, (d) $\Delta = 0.6$ Å, (e) $\Delta = 0.9$ Å, and (f) $\Delta = 1.2$ Å. The unit for the wave vector is the inverse Bohr radius $(1/a_0)$.

doped free-standing graphene [14,15]. Figure 2(b) shows the ELF intensities in LiC_2 when it is located at the equilibrium distance ($\Delta = 0$) from the Ir(111) surface. It turns out that the metallic surface radically modifies the intensities of the electronic modes in LiC_2. Namely, the DP signal becomes very weak and changes to a linearly dispersive mode due to efficient metallic screening in the substrate [50,51], while the AP mode disappears completely. Hence the strong metallic screening produced by the Ir(111) slab dramatically reduces the intensity of the electronic modes and pushes them toward lower energies. In order to clarify the situation, in Figs. 2(c)–2(e) we show the ELF spectra of the LiC_2/Ir(111) systems, where the separation between the LiC_2 and Ir(111) films is gradually increased, from $\Delta = 0.3$ to 1.2 Å.

Figure 2(c) shows that even small upward displacement with $\Delta = 0.3$ Å from the equilibrium causes substantial increase of the DP intensity, while the dispersion remains linear. For $\Delta = 0.6$ Å in the ELF shown in Fig. 2(d) the broad AP peak appears in the lower-energy region due to a less efficient dynamical screening in the substrate [52,53] and the DP signal becomes notably stronger. Already for this separation the intensity of the AP peak is an order of magnitude stronger than the intensity of the AP in free-standing LiC_2 [see Fig. 2(a)]. For $\Delta = 0.9$ Å shown in Fig. 2(e) the dispersion relation of the DP bends (i.e., it is no longer linear) and its energy and intensity increase. The AP becomes a strong, sharp, and well-defined plasmon mode with intensity two orders of magnitude larger than in free-standing LiC_2 and even stronger than the corresponding DP. For $\Delta = 1.2$ Å, shown in Fig. 2(f), the AP intensity reduces by an order of magnitude (in comparison with the $\Delta = 0.9$ Å case) and the DP intensity continues to increase toward its free-standing ($\Delta = \infty$) value. It is important to note that, since the metallic screening reduces the plasmon frequency, it pushes the DP out of the interband $\pi \rightarrow \pi^*$ continuum [54], which in turn reduces the Landau damping and increases the intensity of the plasmon compared to the free-standing case (e.g., compare the intensities in Figs. 2(e) and 2(f) with the intensities in Fig. 2(a) when $Q > 0.1$ a.u.). Here we also have to mention the influence of the intraband $\pi^* \rightarrow \pi^*$ electron-hole excitations on the AP intensity in LiC_2/Ir(111). In the self-standing sample ($\Delta \rightarrow \infty$) the linear AP follows the upper edge of the intraband $\pi^* \rightarrow \pi^*$ continuum $v_F Q$, where v_F is the Fermi velocity in graphene [12]. However, considering that the vicinity of a metallic surface pushes the AP toward lower frequencies (i.e., it decreases the slope of the AP dispersion), for some smaller separations Δ it can be fully immersed in the intraband $\pi^* \rightarrow \pi^*$ continuum. This causes the substantial damping of the AP in LiC_2 deposited on the Ir(111) surface by the intraband $\pi^* \rightarrow \pi^*$ excitations, so in EELS it appears as a broad peak. This effect can be clearly seen in Fig. 2(d).

Also, we note that for the shown momentum-transfer interval the ELF intensities are almost isotropic, i.e., $S(\mathbf{Q}_{\Gamma M}, \omega) \approx S(\mathbf{Q}_{\Gamma K}, \omega)$.

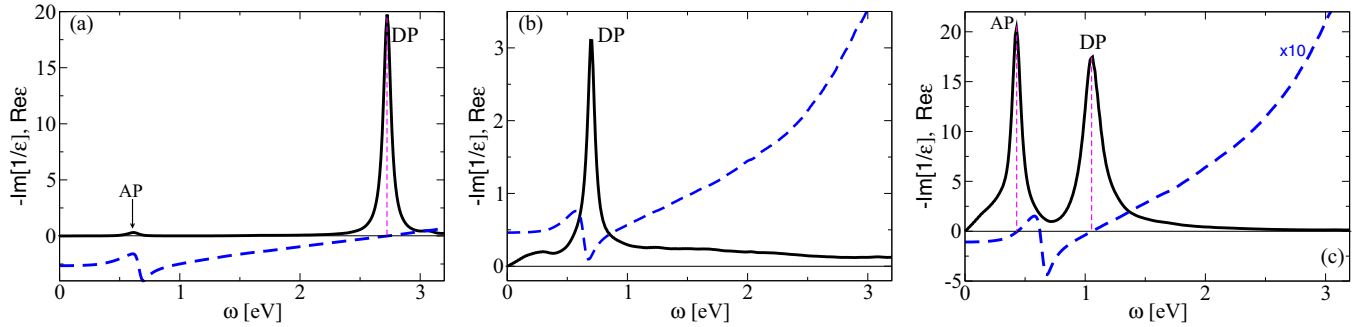

FIG. 3. The energy-loss function (black solid) and Re[ϵ] (blue dashed) in LiC_2/Ir(111) composite for (a) $\Delta = \infty$, (b) $\Delta = 0$, and (c) $\Delta = 0.9$ Å. The momentum-transfer vector with magnitude $Q = 0.054$ a.u. is chosen to be in the Γ-M direction.

The panels in Fig. 2 clearly show that when the LiC_2-Ir(111) distance is out of equilibrium with $\Delta > 0$ the Ir(111) surface induces the strong AP but only for small intervals of separation $0.5 < \Delta < 1.0$ Å. In order to understand such behavior, in Fig. 3 we show the real part of the effective 2D dielectric function (blue dashed lines) for three characteristic separations (a) $\Delta = \infty$, (b) $\Delta = 0$, and (c) $\Delta = 0.9$ Å and for $Q = 0.054$ a.u. in the Γ-M direction. The corresponding ELFs are shown by black solid lines. It can be seen that in all the cases the Re[ϵ] contains a "kink" structure which, depending on the Δ magnitude, shifts up and down as well as crosses zero at different frequencies. For $\Delta = \infty$ the kink, where the weak AP appears, is entirely below zero. At the higher frequencies, i.e., after the kink, the Re[ϵ] increases and crosses the zero where the strong DP appears, classifying the DP as a well-defined collective electronic mode. On the other hand, when $\Delta = 0$ the kink locates entirely above zero and Re[ϵ] does not cross zero at all. This results in the appearance of the weak DP peak around the dip in Re[ϵ]. Considering that when $\Delta = \infty$ changes to $\Delta = 0$ the kink in Re[ϵ] transforms from entirely below to entirely above zero, there should be some Δ interval when the kink crosses zero. As can been seen in Fig. 3(c) this situation occurs, e.g., when $\Delta = 0.9$ Å, resulting in the appearance of both the AP and the DP peaks. In this case both plasmons can be classified as strong well-defined collective modes, as is clear from Fig. 2(e). For slightly larger separation, i.e., $\Delta > 1.0$, the kink falls entirely below zero and the AP signal quickly weakens. However, Re[ϵ] continues to cross zero at larger frequencies where the strong DP appears, as seen in Fig. 2(f).

In Fig. 4(a) we show the ELF intensity of the free-standing ($\Delta = \infty$) CsC_8 layer. In this system the graphene π^* band crosses the Fermi level twice, which together with the partially filled parabolic Cs(σ) band [13] is sufficient for the appearance of the three plasmons, i.e., the strong DP and the two weak acoustic plasmons, which we dub AP_1 and AP_2. This nomenclature for acoustic plasmons is merely a formality, since their dispersion over the entire momentum-transfer range cannot be necessarily linear [15]. Figure 4(b) shows the ELF intensity in CsC_8 when it is at equilibrium distance ($\Delta = 0$) from the Ir(111) surface. The strong metallic screening extremely weakens the oscillatory strengths of the electronic modes such that the DP and AP_2 become weak and barely visible modes, while AP_1 disappears. Figures 4(c)–4(e) show the ELF intensities in CsC_8 when the separation between CsC_8 and the Ir(111) surface gradually increases, from $\Delta = 0.4$ to 1.6 Å. For the $\Delta = 0.4$-Å case presented in Fig. 4(c) the ELF intensity slightly increases. However, at $\Delta = 0.8$ Å the enhancement of the ELF intensity in Fig. 4(d) is already significant and a new AP_1 plasmon appears. It can be noticed that AP_1 and AP_2 have square-root dispersions, which is especially visible in the Γ-M direction. In the Γ-K direction, AP_1 is still a very broad emerging mode. For $\Delta = 1.2$ Å in the ELF shown in Fig. 4(e) the strong AP_1 and AP_2 peaks signal well-defined plasmon modes. In the Γ-K direction AP_1 and AP_2 have well-separated dispersion relations, while in the Γ-M direction and for the larger momentum transfers $Q > 0.1$ a.u. these modes are degenerate. An interesting feature occurs in long-wavelength limit $Q \approx 0$, especially in the Γ-M direction, where AP_2 and the DP start as a one plasmon branch and then at $Q \approx 0.025$ a.u. they bifurcate, i.e., the DP continues as a square-root branch and AP_2 continues as a linear branch. For $\Delta = 1.6$ Å shown in Fig. 4(f) AP_1 is already notably weakened; AP_2 is still a very strong mode, especially for larger momentum transfers $Q > 0.1$ a.u. in both the Γ-M and Γ-K directions; while the DP continues to strengthen. The observable bifurcation into AP_2 and DP branches is still present, in both directions for $Q \approx 0.05$ a.u. As already discussed, in the LiC_2 case, for $\Delta > 2$ Å AP_1 and AP_2 suddenly weaken and the DP becomes gradually stronger until its intensity reaches the freestanding ($\Delta = \infty$) value.

In order to understand the appearance of the strong acoustic plasmons AP_1 and AP_2 in CsC_8 for certain separations Δ, in Fig. 5 we show the real parts (blue dashed lines) of the effective 2D dielectric function (Re[ϵ]) for three characteristic separations (a) $\Delta = \infty$, (b) $\Delta = 0$, and (c) $\Delta = 1.3$ Å, and for $Q = 0.094$ a.u in the Γ-K direction. The ELFs are shown by the black solid lines. Contrary to the LiC_2 case, it can be seen that the Re[ϵ] of CsC_8 has two kinks which move up and down depending on the separation Δ. This means that for certain separations Δ the Re[ϵ] can cross zero three times, and, therefore, three well-defined plasmons appear. Figure 5(a) shows that both kinks are entirely below zero, which gives only weak plasmons. For larger frequencies, after the kink structures, Re[ϵ] crosses zero, providing a relatively strong but quite broad DP. This is reasonable considering that for this momentum transfer the DP already enters the $\pi \rightarrow \pi^*$ interband continuum and is thus considerably Landau damped [54]. This effect can also be seen as a sudden decrease of DP intensity for $Q > 0.05$ a.u. in Fig. 4(a). For $\Delta = 0$ the kinks

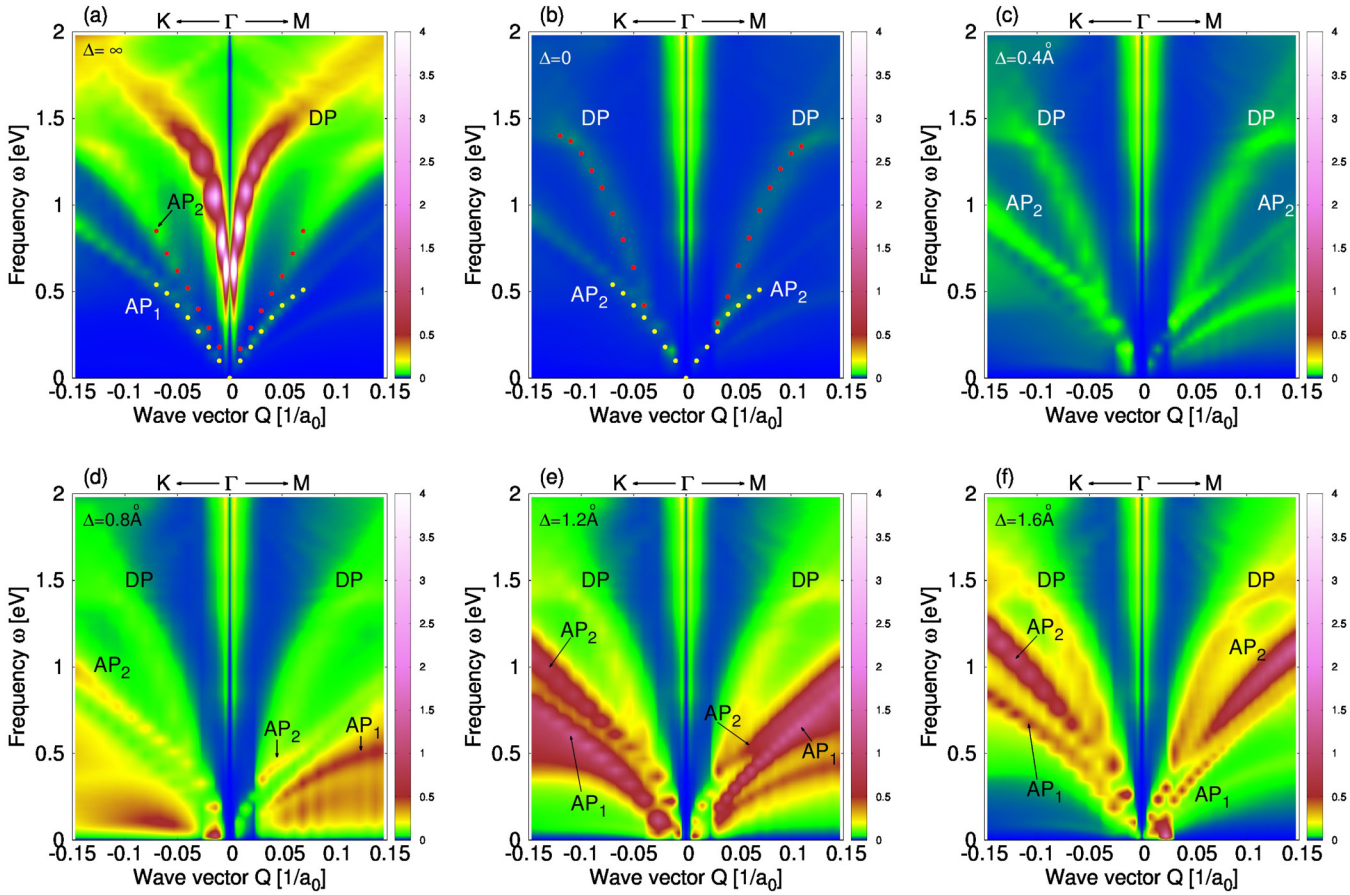

FIG. 4. The energy-loss-function intensity in CsC_8/Ir(111) composite for (a) $\Delta = \infty$, (b) $\Delta = 0$, (c) $\Delta = 0.4$ Å, (d) $\Delta = 0.8$ Å, (e) $\Delta = 1.2$ Å, and (f) $\Delta = 1.6$ Å. The wave-vector unit is inverse Bohr radius ($1/a_0$).

are entirely above zero and Re[ϵ] does not cross zero at all. This results in only two very weak plasmons AP_2 and the DP around which the dips of the kink structures appear. Mapping the conclusions from the LiC_2 case, we expect a narrow Δ interval as well for CsC_8 where at least one of the kinks crosses zero. It should also be noted that for this system there is no Δ for which both kinks would cross zero simultaneously. Figure 5(c) shows that for $\Delta = 1.3$ Å the first kink crosses zero two times, which results in strong and well-defined plasmons AP_1 and AP_2. The second kink is still above zero, resulting in a weak DP just below the dip in the kink. This corresponds to the situation shown in Fig. 4(e) where the two strong plasmons, i.e., AP_1 and AP_2, and the weak DP bands are present. It is important to note here that for $\Delta = 1.3$ Å [Fig. 5(c)] the intensities of AP_1 and AP_2 are an order of magnitude larger than AP_1 and AP_2 intensities and more than two times larger than the DP intensity in CsC_8 for equilibrium separation $\Delta = 0$ [Fig. 5(c)], at the same momentum transfer Q. For slightly larger $\Delta > 2.0$ Å both kinks fall below zero and AP_1 and AP_2 quickly weaken, however Re[ϵ] continues to cross zero for larger frequencies where the stronger DP is present (not shown).

These results generally show that for a narrow interval of displacements [i.e., 0.5 Å $\leqslant \Delta \leqslant$ 1.0 Å for LiC_2/Ir(111)

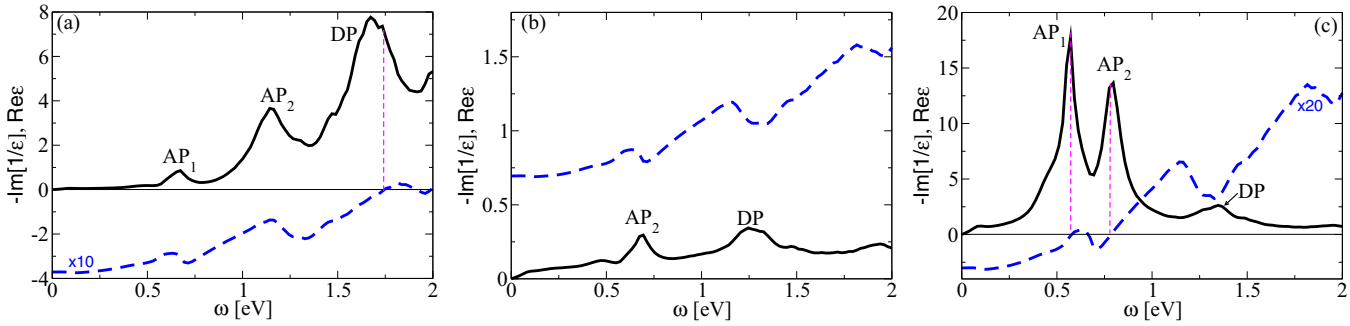

FIG. 5. The energy-loss-function (black solid) and Re[ϵ] (blue dashed) in CsC_8/Ir(111) composite for (a) $\Delta = \infty$, (b) $\Delta = 0$, and (c) $\Delta = 1.3$ Å. The momentum-transfer vector with magnitude $Q = 0.094$ a.u. is chosen to be in the Γ-K direction.

and 1.0 Å $\leqslant \Delta \leqslant$ 1.5 Å for CsC_8/Ir(111)] the AC_x/Ir(111) composites support strong APs, which are for small momentum transfers (i.e., $Q < 0.05$ a.u.) as strong as the DP in the free-standing cases. These APs persist as strong well-defined collective modes in a wide momentum-transfer interval (i.e., $0 < Q < 0.15$ a.u.) such that for larger momentum transfers ($Q > 0.1$ a.u.) APs may be even three orders of magnitude stronger [see Figs. 2(e), 2(f), 4(e), and 4(f)] than the Landau damped DPs in free-standing systems [see Figs. 2(a) and 4(a)]. The metallic screening pushes the DP towards lower frequencies such that in the LiC_2/Ir(111) composite the DP leaves the interband $\pi \rightarrow \pi^*$ continuum and becomes a sharp long-lived mode. Achieving these very interesting plasmonic features requires an artificial ejection of AC_x/Ir(111) from the equilibrium distance Δ which might be experimentally feasible, for instance, by placing an inert single layer or a few layers of hexagonal boron nitride between graphene and the metal surface, as is actually the case in contemporary graphene-based devices [22,23], or by replacing the alkali-metal atoms by larger intercalants, such as the $FeCl_3$ molecules that act as electron acceptors lowering the Fermi energy below -1 eV [55]. Furthermore, the desirable plasmonic properties could be even achieved by changing the concept of the composite system. For example, instead of using metallic substrate one can use insulating substrates (e.g., SiO_2), while the plasmonic properties in the AC_x-substrate heterostructure could be manipulated by a dull metallic (e.g., aluminum) tip from above.

Finally, it should be recalled here that for all separations Δ the noninteracting electron response functions $\chi^0_{AC_x}$ are calculated such that we fix $d_{A\text{-}C}$ separations and Fermi energies E_F to their self-standing values ($h \rightarrow \infty$), as stated in the first two columns of Table I. Thus, the studied modifications of AC_x plasmonics are only due to long-range Coulomb interaction with the Ir(111) surface. The small modification of separation $d_{A\text{-}C}$ and Fermi energy E_F, consequently, with Δ has a minor impact on qualitative plasmonic properties, e.g., DP linearization and AP enhancement. The only expected quantitative effect is weak reduction of DP energy.

IV. CONCLUSIONS

We have demonstrated how the 2D collective modes in chemically doped graphene are drastically modified in the presence of the Ir(111) metallic surface. For instance, a very strong Dirac plasmon present in LiC_2 becomes two orders of magnitude weaker and linearly dispersive, while the acoustic plasmon disappears. Similar modifications were also observed in CsC_8. Further, to understand these physical phenomena we gradually increased the graphene-surface separations Δ and analyzed the effective 2D dielectric function ϵ. We have found that for the equilibrium separation ($\Delta = 0$) the strong metallic screening pushes the real part of the effective 2D dielectric function (Re[ϵ]) entirely above zero, which blocks the formation of well-defined 2D collective modes. However, for a narrow interval of out-of-equilibrium separations ($\Delta > 0$) Re[ϵ] crosses zero twice, providing two strong 2D plasmons. In particular, for 0.5 Å $\leqslant \Delta \leqslant$ 1.0 Å the LiC_2/Ir(111) composite supports strong well-defined Dirac and acoustic plasmons, while for 1.0 Å $\leqslant \Delta \leqslant$ 1.5 Å the CsC_8/Ir(111) composite contains two intense acoustic plasmons when the momentum-transfer magnitude is smaller than 0.15 a.u. All in all, we have shown that chemically doped graphene in the presence of a metallic surface could support even superior plasmonic features compared to the freestanding case. This manipulative plasmonic property can be used in many applications such as biosensing or in plasmon enhanced spectroscopic techniques.

ACKNOWLEDGMENTS

V.D. acknowledges support from the QuantiXLie Center of Excellence, a project cofinanced by the Croatian Government and European Union through the European Regional Development Fund within the Competitiveness and Cohesion Operational Programme (Grant No. KK.01.1.1.01.0004). V.D. is also grateful to Donostia International Physics Center (DIPC) for hospitality during various stages of this work. D.N. acknowledges financial support from the European Regional Development Fund for the "Center of Excellence for Advanced Materials and Sensing Devices" (Grant No. KK.01.1.1.01.0001). I.L. acknowledges support from the European Union through the European Regional Development Fund within the Competitiveness and Cohesion Operational Programme (Grant No. KK.01.1.1.06). V.M.S. acknowledges partial support from the Spanish Ministry of Economy and Competitiveness MINECO Grant No. FIS2016-76617-P and from Project No. PI2017-30 of the Departamento de Educación, Política Lingüística y Cultura of the Basque government. Computational resources were provided by the DIPC Computing Center.

[1] P. Pervan, P. Lazić, M. Petrović, I. Š. Rakić, I. Pletikosić, M. Kralj, M. Milun, and T. Valla, Phys. Rev. B **92**, 245415 (2015).

[2] J. Halle, N. Neel, and J. Kroger, Phys. Chem. C **120**, 5067 (2016).

[3] M. Petrović, I. Šrut Rakić, S. Runte, C. Busse, J. T. Sadowski, P. Lazić, I. Pletikosić, Z.-H. Pan, M. Milun, P. Pervan, N. Atodiresei, R. Brako, D. Šokčević, T. Valla, T. Michely, and M. Kralj, Nat. Commun. **4**, 2772 (2013).

[4] S. Tanaka, M. Petrović, K. Watanabe, P. Lazić, M. Kralj, T. Sugimoto, and Y. Matsumoto (unpublished).

[5] S. Schumacher, T. Wehling, P. Lazić, S. Runte, D. F. Forster, C. Busse, M. Petrović, M. Kralj, S. Blügel, N. Atodiresei, V. Caciuc, and T. Michely, Nano Lett. **13**, 5013 (2013).

[6] B. Cook, A. Russakoff, and K. Varga, Appl. Phys. Lett. **106**, 211601 (2015).

[7] M. Alattas and U. Schwingenschlogl, Sci. Rep. **6**, 26753 (2016).

[8] D. Novko, Nano Lett. **17**, 6991 (2017).

[9] I. Lončarić, Z. Rukelj, V. M. Silkin, and V. Despoja, npj 2D Mater. and Appl. **2**, 33 (2018).

[10] B. Wunsch, T. Stauber, F. Sols, and F. Guinea, New J. Phys. **8**, 318 (2006).

[11] E. H. Hwang and S. Das Sarma, Phys. Rev. B **75**, 205418 (2007).

[12] L. Marušić and V. Despoja, Phys. Rev. B **95**, 201408(R) (2017).

[13] V. Despoja and L. Marušić, Phys. Rev. B **97**, 205426 (2018).

[14] Y. Gao and Z. Yuan, Solid State Commun. **151**, 1009 (2011).

[15] M. Pisarra, A. Sindona, P. Riccardi, V. M. Silkin, and J. M. Pitarke, New J. Phys. **16**, 083003 (2014).

[16] H. Pfnür, T. Langer, J. Baringhaus, and C. Tegenkamp, J. Phys.: Condens. Matter **23**, 112204 (2011).

[17] T. Langer, D. F. Forster, C. Busse, T. Michely, H. Pfnür, and C. Tegenkamp, New J. Phys. **13**, 053006 (2011).

[18] A. Cupolillo, A. Politano, N. Ligato, D. M. C. Perez, G. Chiarello, and L. S. Caputi, Surf. Sci. **634**, 76 (2015).

[19] A. Politano, H. K. Yu, D. Farías, and G. Chiarello, Phys. Rev B **97**, 035414 (2018).

[20] A. Principi, E. van Loon, M. Polini, and M. I. Katsnelson, Phys. Rev. B **98**, 035427 (2018).

[21] A. R. Echarri, J. D. Cox, and F. J. García de Abajo, Optica **6**, 630 (2019).

[22] M. B. Lundeberg, Y. D. Gao, R. Asgari, C. Tan, B. Van Duppen, M. Autore, P. Alonso-Gonzalez, A. Woessner, K. Watanabe, T. Taniguchi, R. Hillenbrand, J. Hone, M. Polini, and F. H. L. Koppens, Science **357**, 187 (2017).

[23] D. A. Iranzo, S. Nanot, E. J. C. Dias, I. Epstein, C. Peng, D. K. Efetov, M. B. Lundeberg, R. Parret, J. Osmond, J.-Y. Hong, J. Kong, D. R. Englund, N. M. R. Peres, and F. H. L. Koppens, Science **360**, 291 (2018).

[24] D. Rodrigo, O. Limaj, D. Janner, D. Etezadi, F. J. García de Abajo, V. Pruneri, and H. Altug, Science **349**, 165 (2015).

[25] M. Pumera, Materials Today **14**, 308 (2011).

[26] E. Singh, M. Meyyappan, and H. S. Nalwa, ACS Appl. Mater. Interfaces **9**, 34544 (2017).

[27] T. Mahmoudi, Y. Wang, and Y.-B. Hahn, Nano Energy **47**, 51 (2018).

[28] Y. Miyoshi, Y. Fukazawa, Y. Amasaka, R. Reckmann, T. Yokoi, K. Ishida, K. Kawahara, H. Ago, and H. Maki, Nat. Commun. **9**, 1279 (2018).

[29] T. Low and P. Avouris, ACS Nano **8**, 1086 (2014).

[30] S. Huang, C. Song, G. Zhang, and H. Yan, Nanophotonics **6**, 1191 (2017).

[31] M. Jablan, H. Buljan, and M. Soljačić, Phys. Rev. B **80**, 245435 (2009).

[32] K. S. Novoselov, V. I. Falko, L. Colombo, P. R. Gellert, M. G. Schwab, and K. Kim, Nature (London) **490**, 192 (2012).

[33] F. Schwierz, Proc. IEEE **101**, 1567 (2013).

[34] F. Xia, Proc. IEEE **101**, 1717 (2013).

[35] M. Jablan, M. Soljačić, and H. Buljan, Proc. IEEE **101**, 1689 (2013).

[36] S. Xiao, X. Zhu, B.-H. Li, and N. A. Mortensen, Front. Phys. **11**, 117801 (2016).

[37] P. Giannozzi, S. Baroni, N. Bonini, M. Calandra, R. Car, C. Cavazzoni, D. Ceresoli, G. L. Chiarotti, M. Cococcioni, I. Dabo *et al.*, J. Phys.: Condens. Matter **21**, 395502 (2009).

[38] P. Giannozzi, O. Andreussi, T. Brumme, O. Bunau, M. B. Nardelli, M. Calandra, R. Car, C. Cavazzoni, D. Ceresoli, M. Cococcioni *et al.*, J. Phys.: Condens. Matter **29**, 465901 (2017).

[39] N. Troullier and J. L. Martins, Phys. Rev. B **43**, 1993 (1991).

[40] I. Lončarić and V. Despoja, Phys. Rev. B **90**, 075414 (2014).

[41] C. Busse, P. Lazić, R. Djemour, J. Coraux, T. Gerber, N. Atodiresei, V. Caciuc, R. Brako, A. T. N'Diaye, S. Blügel, J. Zegenhagen, and T. Michely, Phys. Rev. Lett. **107**, 036101 (2011).

[42] K. Berland, C. A. Arter, V. R. Cooper, K. lee, B. I. Lundqvist, E. Schroder, T. Thonhauser, and P. Hyldgaard, J. Chem. Phys. **140**, 18A539 (2014).

[43] P. Hyldgaard, K. Berland, and E. Schroder, Phys. Rev. B **90**, 075148 (2014).

[44] H. J. Monkhorst and J. D. Pack, Phys. Rev. B **13**, 5188 (1976).

[45] DFT calculations of separate layers are performed in the same way as for the complete system, except the XC potential in LiC_2 is approximated by the Perdew-Zunger local-density approximation [46] and that in CsC_8 and the Ir(111) surface is approximated by the Perdew-Burke-Ernzerhof generalized gradient approximation [47]. We used $12 \times 12 \times 1$, $6 \times 6 \times 1$, and $12 \times 12 \times 1$ Monkhorst-Pack K-point mesh for LiC_2, CsC_8, and Ir(111), respectively. Supercells in the z direction for AC_x are set to 12.3 Å and those for the Ir(111) surface are set to 20.9 Å.

[46] J. P. Perdew and A. Zunger, Phys. Rev. B **23**, 5048 (1981).

[47] J. P. Perdew, K. Burke, and M. Ernzerhof, Phys. Rev. Lett. **77**, 3865 (1996).

[48] V. Despoja, Z. Rukelj, and L. Marušić, Phys. Rev B **94**, 165446 (2016).

[49] V. U. Nazarov, New J. Phys. **17**, 073018 (2015).

[50] J. M. Pitarke, V. U. Nazarov, V. M. Silkin, E. V. Chulkov, E. Zaremba, and P. M. Echenique, Phys. Rev. B **70**, 205403 (2004).

[51] B. Diaconescu, K. Pohl, L. Vattuone, L. Savio, P. Hofmann, V. M. Silkin, J. M. Pitarke, E. V. Chulkov, P. M. Echenique, D. Farías, and M. Rocca, Nature (London) **448**, 57 (2007).

[52] V. M. Silkin, A. García-Lekue, J. M. Pitarke, E. V. Chulkov, E. Zaremba, and P. M. Echenique, Europhys. Lett. **66**, 260 (2004).

[53] L. Vattuone, M. Smerieri, T. Langer, C. Tegenkamp, H. Pfnür, V. M. Silkin, E. V. Chulkov, P. M. Echenique, and M. Rocca, Phys. Rev. Lett. **110**, 127405 (2013).

[54] V. Despoja, D. Novko, K. Dekanić, M. Sunjić, and L. Marušić, Phys. Rev. B **87**, 075447 (2013).

[55] F. J. Bezares, A. De Sanctis, J. R. M. Saavedra, A. Woessner, P. Alonso-Gonzalez, T. Amenabar, J. N. Chen, T. H. Bointon, S. Y. Dai, M. M. Fogler, D. N. Basov, R. Hillenbrand, M. F. Craciun, F. J. García de Abajo, S. Russo, and F. H. L. Koppens, Nano Lett. **17**, 5908 (2017).